Photoelectrochemical mineralization of emerging contaminants at porous WO_3 interfaces

Gelsomina Longobucco

Luisa Pasti*
luisa.pasti@unife.it

Alessandra Molinari

Nicola Marchetti

Stefano Caramori*
cte@unife.it

Vito Cristino

Rita Boaretto

Carlo Alberto Bignozzi*
g4s@unife.it

Department of Chemical and Pharmaceutical Sciences of the University of Ferrara, Via Fossato di Mortara 17, 44121, Ferrara, Italy, Italy (Italy is typed twice, delete one)

*Corresponding author.

Abstract

Nanocrystalline WO_3 absorbs visible light up to 470 nm and generates OH
•
radicals via valence band injection. Therefore, it promotes the OH
•
mediated oxidation of organic pollutants, when applied to the near UV–vis photodegradation of environmentally relevant target molecules like atenolol and carbamazepine. They both represent potentially hazardous recalcitrant contaminants of emerging concern (CEC) in waters. In the case of WO_3 electrodes, a considerable acceleration of the degradation kinetics (up to 4–5 times) occurs through the application of a 1.5 V potential bias, which is instrumental to optimize the charge separation within the thin films and to maximize holes transfer rate to the electrolyte. Moreover, after sufficiently long irradiation, the complete mineralization of the organics is obtained. Interestingly, the photo-electrochemical degradation process (applied bias condition) maintains its effectiveness and a large efficiency margin over conventional open circuit conditions. Photoelectrocatalysis is observed even in diluted supporting electrolyte conditions, representing the average salinity of natural freshwater samples, demonstrating the advantageous practical feasibility of the photo-electrochemical approach.

Keywords: Drug mineralization; Environmental contaminants; Hydroxyl radicals; Photo-electrocatalysis; Tungsten trioxide

1 Introduction

The use of semiconductor materials represents one of the most promising way to harvest solar energy resulting in the production of charge carriers with unitary (Change "unitary" with 100%) quantum yield (i.e. every absorbed photon results in the formation of an electron/hole pair) [1,2]. These carriers can be used to drive redox reactions at the semiconductor interface in contact with either liquid electrolytes, vapor or gas phases, triggering the direct conversion of solar energy into chemical energy. Both the yield of the fuel forming reactions in photo-electrochemical cells, where oxygen and hydrogen result from the splitting of the water molecule, and the efficiency of the photocatalytic pathways, concerning either the demolition of environmental contaminants or the production of useful chemical intermediates, are primarily dependent on the

competition between interfacial charge transfer and recombination. Charge trapping events and the specific chemical nature of intermediates generated at the semiconductor surface are also important in determining the kinetic and mechanism of charge separation.

Among wide band gap semiconductors, WO_3 represents a good compromise between sun harvesting capabilities, allowing to capture visible photons up to 450–480 nm, and band edge energy levels which are suitable to drive demanding oxidation reactions, among which water photo(change "photooxidation" with "photo-oxidation")oxidation attracted most of the interest [3]. Thus, WO_3 was often studied in the framework of photo-electrochemical cells (PEC) for solar water splitting, representing the anodic component of the PEC cell. WO_3 can be prepared in the form of either transparent or opaque thin films by applying a variety of techniques aimed at the production of nanostructured interfaces, which optimize the interfacial area [4] as well as electrical interconnection among the nanoparticles/nanostructures. These methods include, but are not limited to, sol-gel, hydrothermal and electrophoretic processes [5–9], electrochemical anodization [10–14], radio frequency (rf) sputtering [15,16], pulsed laser deposition [17] and evaporation [18].

Although it is often assumed that oxygen evolves at the WO_3 surface following illumination and water photo-oxidation occurs(change "occurs at anodic potential" with "occurring under anodic bias") at anodic potentials [19], Mi et al. [20], by using a luminescent probe, found nearly no oxygen evolved in sulfate containing electrolytes, pointing out that the oxidation of the anions may be the predominant hole scavenging pathway in acidic conditions. Intrigued by such finding, we have recently undertook a study [21] where it could be demonstrated, by combining conventional DC and AC photo-electrochemical investigations, Electronic Paramagnetic Resonance (EPR), photo-electrochemical oxygen evolution measurements and Transient Absorption Spectroscopy, that following reaction of photo-holes with the aqueous medium, $OH^{\bullet}$ radicals are the primary intermediates produced at the WO_3 surface. Thus, oxidation of organic and inorganic species (i.e. hole scavengers) at the WO_3 surface is likely to occur according to a $OH^{\bullet}$ mediated mechanism rather than by direct reaction with photo-holes. It was also found that the charge transfer occurs through the valence band, consistent with the demanding $OH^{\bullet}$ generation energetics, and that the voltage drop across the WO_3/solution interface mainly involves the space charge layer of the semiconductor, controlling the resulting photoanodic current via potential-induced variations of hole density at the surface of WO_3. Thus, a substantial acceleration of $OH^{\bullet}$ radical generation could be envisioned under photo-electrochemical conditions in the presence of anodic potential bias.

These findings point out the possibility to apply WO_3 photoanodes to two different contexts of great interest:

1) photoelectrolysis in aqueous solutions containing concentrated organic species, resulting in a large (ca. twice) increase of the photoanodic current generated from photo(change "photooxidation" with "photo-oxidation")oxidation of the organics, boosting hydrogen production at the cathodic compartment of the cell. This process is clearly coupled to COD (Chemical Oxygen Demand) abatement and has been observed to occur with a number of organic scavengers including methanol, formic acid, triethanol-amine, glucose, alkyl-ammonium salts etc. [22,23];

2) photoelectrolytic processes in diluted solutions, where no significant improvement in the photoanodic current will be observed, but it will persist the possibility to employ photo-generated $OH^{\bullet}$ radicals to demolish organic pollutants present in ppm concentration. These contaminants may have a significant kinetic barrier for the direct electrochemical or photo-electrochemical oxidation and could be impervious to other conventional decontamination methods.

The possibility of carrying out a photoelectrolytic water decontamination in diluted aqueous solutions with respect to both electrolyte and contaminant target concentrations has been rarely considered [24,25], and to the best of our knowledge, not in the case of WO_3. Nevertheless, it is an application of great relevance in the framework of the protection of water resources, of fresh and salt water ecosystems worldwide. In view of the rising world industrialization paralleled by the increment of world population, particularly in water scarce countries, the re-use of wastewaters will be necessarily an increasing practice, which, however, is not without drawbacks, bringing potential health risks due to the presence of highly toxic organic pollutants. In particular, the contaminants of emerging concerns (CECs), which include pharmaceuticals, detergents and hormones, were proved challenging for conventional wastewater and recycled water treatments, which are only partially effective in their removal or degradation [26]. CECs are so discharged into the environment where they may have adverse long-term impact on both human health and life of aquatic organisms.

In this contribution, we report on the photo-electrochemical degradation under visible light of pharmaceuticals of emerging environmental concern comprising atenolol (ATN) and carbamazepine (CBZ) (Scheme 1). ATN, a beta-blocker, and CBZ, a psychoactive drug, were selected for being some of the most representative contaminants.

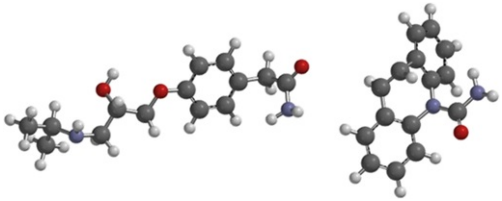

Scheme 1 Computed equilibrium structures obtained at the PM3-DFT-6-31G* level in vacuo of: atenolol (ATN), left; carbamazepine (CBZ), right.

alt-text: Scheme 1

In particular, CBZ is one of the most persistent pharmaceuticals of concern in water bodies that receive wastewater effluent and its resistance to degradation makes CBZ an indicator of both wastewater influx into streams and exfiltration from sewers [27]. Likewise, ATN for its resistance to decontamination processes has been selected as an indicator compound representing potential contamination from other pharmaceuticals and can gauge the efficacy of treatment processes [28,29]. The degradation pathway of these pollutants was investigated by means of HPLC-MS analysis, which evidenced that the oxidation products originate by the initial hydroxylation of the target molecules, probably following hydrogen abstraction from the C-H groups. Interestingly, under photoelectrochemical conditions, when a positive bias was applied to the semiconductor working electrode, the degradation kinetics of these pollutants were greatly accelerated, resulting in their complete mineralization under visible light even at pH and ionic strength conditions similar to those of real samples.

2 Experimental

2.1 Chemicals for ~~Analytical and Photo-electrochemical M~~analytical and photo-electrochemical measurements

Carbamazepine (purity 99%), atenolol (purity 98.5%), sodium perchlorate (purity 98%), sodium sulfate (purity 99%), perchloric acid (70%) and sulfuric acid (95%) reagent grade were purchased from Sigma-Aldrich (Sigma-Aldrich, Srl, Italy) and used as received. High-performance liquid chromatography (HPLC) grade acetonitrile (ACN) was purchased from Merck (Darmstadt, Germany). The water employed was Milli-Q® grade (Millipore, MA, USA).

Dilute aqueous solutions of perchloric acid and sulfuric acid were employed to adjust the pH (pH = 3 or 6) of the drug solutions, containing 0.1 M sodium perchlorate or 0.1 M (or 0.7 mM) sodium sulfate as electrolyte, respectively. The pH of the drugs solutions was measured with a combined glass electrode connected to an AMEL pHmeter (Milano, Italy).

2.2 Nanocrystalline WO_3 powder synthesis and photoanodes preparation

Nanocrystalline WO_3 was prepared by following a published procedure [30]. Briefly, H_2WO_4 was generated from Na_2WO_4 (Alfa Aesar) by addition of concentrated HCl (Aldrich), followed by several washings in order to eliminate NaCl. The colloidal suspension of H_2WO_4 was obtained by addition of oxalic acid (Aldrich). The WO_3 powder was obtained by firing at 550 °C for 1 h in air the H_2WO_4 colloid. Before use in photocatalytic experiments, the resulting WO_3 crystalline powder was ball mill homogenized (20 min at 40 rpm).

Two different types of photoanodes were tested. A) Colloidal WO_3.(change WO_3 with WO_3.) Transparent nanocrystalline electrodes cast onto well cleaned FTO (Pilkington TEC 8) glass were prepared by sequential spin coating deposition of the H_2WO_4 precursor prepared by adding 20% w/w Carbowax (Aldrich, 15000–20000 u) and triton X-100 (Fluka) (1 drop/2 g of colloidal precursor) to the H_2WO_4/oxalic acid colloid [21]. After each deposition the electrode was heated at 550 °C for 30 min~~utes~~ in air. Up to six spin coated layers afforded nanocrystalline electrodes having a thickness of ca. 1.5 µm. All electrodes have active area of 1 cm^2.

B) Anodized WO_3.(change WO_3 with WO_3.) WO_3 films on tungsten foils were prepared by accelerated potentiostatic anodization as described elsewhere [21,31]. Shortly, well cleaned tungsten sheets (Alfa Aesar, 2 × 0.5 cm active area) were immersed in a NMF based electrolyte (~~N~~*N*-methyl-formamide (Alfa Aesar)/water 80/20 v/v + 0.05% w/w NH_4F (Alfa Aesar)) and subjected to potentiostatic anodization in a two electrode configuration at 40 V for 7 h~~ours~~ at 40 °C. The resulting films were washed and sonicated in water and then annealed in air at 550 °C for 1 h. Nanocrystalline porous oxide layers ca. 2 µm thick were obtained.

2.3 Structural and morphological ~~C~~characterization of WO_3

AFM measurements were carried out with a Digital Instruments Nanoscope III scanning probe Microscope (Digital Instruments, CA). The instrument was equipped with silicon tip (RTESP-300 Bruker) and operated in tapping mode. The scan size was 3 µm at a frequency of 1 Hz and a resolution of 512 samples/line. Flattening and surface topographical analysis of raw AFM images was carried out with NanoScope Analysis 1.5 program.

X-ray diffraction (XRD) on WO_3 powders was carried out with a Bruker D8 Advance diffractometer by using the monochromatic Cu Kα radiation with a stepsize of 0.02° and a step time of 2 s. XRD of the thin film

photoelectrodes was carried out at grazing incident angle (3° for the colloidal film and 1.5° for the anodic film) with a stepsize of 0.02° and a steptime of 15.02 s. Scanning Electron Microscopy (SEM) imaging was obtained with a Zeiss Evo 40 electron microscope.

2.4 Photocatalytic experiments

2.4.1 Suspensions

WO_3 crystalline powder (10 mg) was suspended and stirred in an aerated aqueous solution (3 mL, pH 3.1) containing atenolol (ATN, C_0 = 10 mg/L) and $NaClO_4$ (0.1 M) and then irradiated (λ> 360 nm) with a Hg medium pressure lamp (15 mW/cm^2, Helios Italquartz) for subsequent times. At the end of irradiation, the sample was centrifuged for 10 min at 4000 rpm (Eppendorf Centrifuge 5418). The supernatant was filtered (filter 0.22 μm PVDF Agilent) and successively analyzed by HPLC DAD for determining the remaining concentration of drug (C).

Analogous experiments were carried out suspending WO_3 in aerated aqueous solutions (pH 5.1) containing carbamazepine (CBZ, C_0 = 10 mg/L) and $NaClO_4$ (0.1 M). In general the same ionic strength was used for both photocatalytic and photoelectrochemical (applied anodic bias) experiments, in order to reproduce the same ionic environment and surface potential for the WO_3 and obtain fully comparable sets of experiments.

2.4.2 Electrodes

colloidal WO_3 or anodized WO_3 (illuminated area = 1 cm^2) photoanodes were placed in a quartz photo-electrochemical cell and immersed in aqueous solutions of ATN or CBZ (C_0 = 10 mg/L) containing $NaClO_4$ (0.1 M) at the desired pH value and then illuminated at normal incidence (λ > 360 nm) in the absence of applied potential bias for subsequent times. At the end of irradiation cycles of the duration of 1, 3 and 5 h, the solution was filtered and analyzed by HPLC DAD. The maximum amount of WO_3 loaded onto an active surface of 1 cm^2, by considering the bulk density of WO_3 (7.16 g/cm^3) is of the order of 0.11 mg, that is ca. 10 times less than the suspended powder.

2.5 Photo-electrocatalytic experiments

Photodegradation experiments under photo-electrochemical conditions were carried out in a two electrode configuration with an Eco Chemie PGSTAT 101 potentiostat/galvanostat running under Nova environment. The same type of electrodes, cell setup and optical configuration described for open circuit photocatalysis was used for photoelectrochemical experiments under applied bias. Visible light illumination (λ > 420 nm) was obtained by using an appropriate cut-off filter (Edmund Optics). Photo-electrochemical experiments were conducted either in aqueous 0.1 M $NaClO_4$ or Na_2SO_4 electrolytes at variable pH, by applying a constant bias of 1.5 V vs a platinum grid counter counter-electrode. The same experiments were repeated in aqueous 0.7 mM Na_2SO_4 at pH 6. The 1.5 V bias was selected in consideration of the limiting photoanodic current observed from the J-V curve of the photoelectrode, of which a typical example is reported as Fig. S1 (see Supporting ~~I~~information (SI)). In the presence of periodic depolarization cycles at 0 V for 10 min~~utes~~ introduced between bias cycles of the duration of 30 min~~utes~~, the photocurrent response of the WO_3 electrodes was stable and reproducible (see Figs. S2 and S3 in SI for the photocurrent response to a typical photo-electrochemical degradation cycle in concentrated (0.1 M) and diluted (0.7 mM) Na_2SO_4 supporting electrolyte). The same electrode could be used for several days without observing any degradation of its J-V characteristics.

IPCE (Incident Photon to Current Conversion Efficiency) spectra were acquired under the monochromatic light generated by an Applied Photophysics Monochromator (bandwidth 10 nm) coupled to a 175 W Luxtel Xenon lamp. Photocurrent generated under a constant potential of 1.5 V was measured with an Agilent 34401A multimeter while monochromatic incident irradiance was obtained with a Centronic calibrated silicon photodiode.

2.6 HPLC DAD analysis

A HPLC/DAD (Waters, MA, USA pump: Waters 515, DAD: Waters PDA 996) was employed under isocratric elution conditions, the eluent was 5:95 ACN: phosphate buffer 2 mM pH = 3 and 30:70 ACN: phosphate buffer 2 mM pH = 3 for ATN and CBZ respectively. The flow rate was 1 mL/min, while the column was thermostated at 25 °C. The column was 150 × 4.6 mm (Phenomenex, CA, USA) and packed with a C18 silica-based stationary phase with a particle diameter of 5 μm. The injection volume was 20 μL for all standards and samples. The detection wavelengths were selected at 224 nm and 285 nm for ATN and CBZ respectively.

2.7 EPR spectroscopy experiments

EPR spin-trapping experiments were carried out with a Bruker ER200 MRD spectrometer equipped with a TE 201 resonator (microwave frequency of 9.4 GHz). The samples were suspensions of WO_3, obtained as reported above, in aqueous solutions containing ATN (10 mg/L, pH 3.1) or CBZ (10 mg/L or 200 mg/L, pH 5.1) and 5,5′ dimethyl-pyrrolin N-oxide (DMPO, 5 10^{-2} M) as the spin trap. The samples were put into a flat quartz cell and directly illuminated in the instrument cavity by a Hg medium pressure lamp (λ > 360 nm). No EPR signals were obtained in the dark and during irradiation of the solution in the absence of WO_3.

2.8 HPLC/MS analysis

HPLC/MS analyses were made by means of Surveyor micro-HPLC hyphenated to a linear trap quadrupole (LTQ) mass spectrometer (LTQ XL Thermo Scientific, Waltham, MA, USA). The HPLC apparatus was composed of a solvent delivery system, a quaternary pump (including a membrane degasser) and an autosampler (including a thermostated column compartment). The LTQ system was equipped with an electrospray ionization (ESI) ion source. The mobile phase was obtained as a mixture of acetonitrile (ACN) formic acid 0.1% v/v: water formic acid 0.1% v/v. Chromatographic separation was performed under gradient elution conditions: 0–6 min 5% ACN, 6–14 min 5–70% ACN, 14–15 min 70% ACN, then held isocratically at 95% of ACN for 3 min before reconditioning the column. The flow rate was 100 µL/min, while the column was thermostated at 25 °C. The column was 50 × 2.1 mm (Restek, Bellefonte, PA, USA) and packed with a C18 silica-based stationary phase with a particle diameter of 3 µm. The injection volume was 5 µL for all standards and samples. MS experimental conditions were as follows: spray voltage 4 kV, capillary temperature 275 °C, capillary voltage 11 V and tube lens 25 V for positive ESI conditions.

3 Results and discussion

3.1 Morphology and structure

All WO_3 samples used for photocatalytic and photoelectrochemical experiments, after 550 °C annealing in air, exhibit a well-defined monoclinic crystalline structure, resulting in the most intense diffraction peaks from the planes (002) (020) (200) (112) and (202) (Fig. S4 in SI). In the case of the anodically grown WO_3, the diffraction peaks are lower in intensity and broader, suggesting the presence of smaller coherent scattering domains. The SEM imaging of the calcined WO_3 powder, obtained from the H_2WO_4 colloidal precursor in the absence of the organic binder/dispersing agents, shows the presence of flat, discoidal particles having a quite homogenous size distribution, with a diameter of 300 ± 100 nm, and a thickness of ca. 100 nm (Fig. S5 in SI). The AFM investigation of the thin films used in the photoelectrochemical processes provides information consistent with previously published results (see Fig. 1): the colloidal films, obtained by repeated (×6) spin casting of the H_2WO_4 precursor in the presence of Carbowax, as organic sintering agent, are characterized by the presence of a homogenous coverage by spherical WO_3 particles having a relatively narrow size distribution centered around 55 nm. By contrast, the anodically grown film is composed by larger, roughly spherical, strongly fused and interconnected particles having a broad polydispersity and average size >100 nm. These substructures constitute ridges and crests of an irregular porous oxide network, which covers completely the underlying metal. The XRD analysis suggests that in this latter case each of the hundred-nanometers sized particle has a polycrystalline nature, formed by smaller crystallites of the size of few tens nanometers [28].

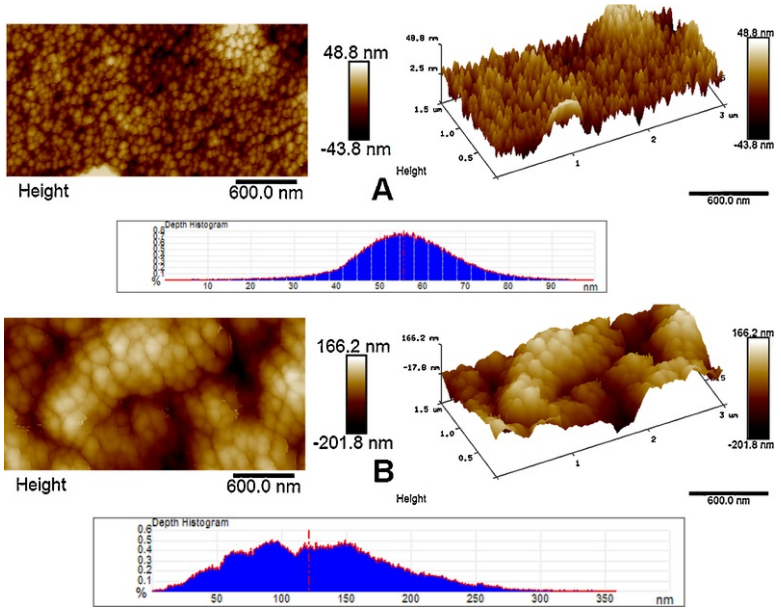

Fig. 1 AFM imaging of the WO_3 photoelectrodes used for photodegradation experiments: A) colloidal WO_3 film. B) Anodically grown WO_3.

alt-text: Fig. 1

3.2 Photocatalytic degradation of drugs by WO_3

Atenolol (ATN) or carbamazepine (CBZ) whose initial concentration (C_0) was 10 mg/L have been dissolved in aerated aqueous solutions containing $NaClO_4$ (0.1 M) and photo-catalytically degraded upon illumination of suspended WO_3 powder. Initially, with atenolol (add "," after "atenolol") an acidic pH (~3), (delete "," before "was") was selected. This pH is well within the stability interval of WO_3 and prevents semiconductor dissolution during photocatalytic experiments of the duration of a few hours. Later, after having verified the WO_3 stability during the photocatalytic process, we have explored higher pH values, closer to those found in natural freshwaters (pH 5–6). Fig. 2(A and B), which shows C/C_0 ratio as a function of irradiation time obtained for WO_3 suspension, reports also the results obtained with the photoactive WO_3 film either deposited on FTO or anodically grown on W foils. It can be seen that drug degradation on WO_3 suspensions is faster than with immobilized WO_3, ostensibly because of a decreased surface area in the sintered films. The observed differences, however, are not enormous. In fact, after 5 h irradiation, the thin films achieve a degradation of ca. 50–60% of the starting ATN and of about 40%–60% of CBZ which compares favorably with values of the order of 70% recorded for both pollutants in the presence of the semiconductor suspension. Fig. 2(A and B) also shows that the two different electrodes (i.e. colloidal and anodized WO_3) display equivalent photocatalytic performances suggesting the possibility of their customized use depending on their intrinsic characteristics. For example, colloidal WO_3 could be best employed to decorate insulating substrates where transparency is important, while the tungsten sintered WO_3 could be best suited for applications demanding conductivity, mechanical flexibility, and resistance to high solar irradiance and temperature. It is obvious that immobilization of WO_3 permits an easy separation of the catalyst from the solution facilitating its reuse.

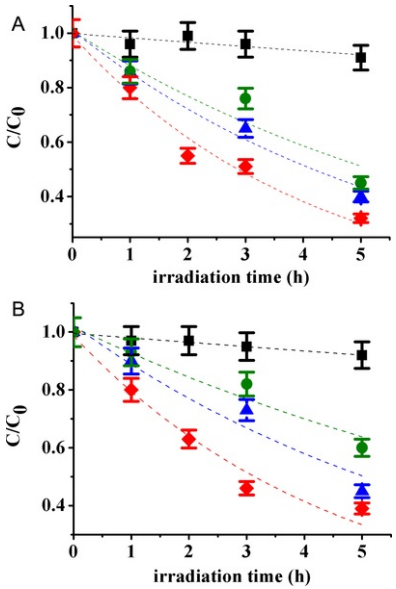

Fig. 2 A) Degradation of ATN (C_0 = 10 mg/L) dissolved in aqueous solution (pH 3.1) containing $NaClO_4$ (0.1 M) by irradiation (λ > 360 nm) of WO_3 in suspension (♦, 3 g/L), of colloidal WO_3 deposited on glass (circles ●) and of anodically grown WO_3 on W foils (triangles ▲). Decrease of ATN in time in the presence of WO_3 in the dark is also reported (■). B) Degradation of CBZ (pH 5.1) under the same conditions described in part A.

alt-text: Fig. 2

Drug concentration variations in the dark, in the presence of WO_3, do not exceed 10% and are probably due to surface adsorption on the semiconductor. In addition, direct irradiation of the drug solution in the absence of WO_3 leads to a negligible degradation, therefore, we conclude that the degradation processes of ATN and CBZ upon irradiation of WO_3 is photocatalytic in nature. The concentration decays of the two drugs were well fitted by a (delete "a") first order kinetics with rate constants in the range 0.1–0.2 h^{-1}, depending on the type of substrate (Table 1) and with correlation coefficients for the first order decays higher than 0.9 for all the investigated species in the different conditions.

Table 1 Estimated kinetics parameters (a, k) of the experimental data to a first order law: $C/C_0 = ae^{-kt}$.

alt-text: Table 1

Experimental conditions	Anodic material	Kinetic parameters	(a) (k, h^{-1})	Standard deviation	Correlation coefficient
ATN,	Colloidal WO_3	a	1.01	0.033	0.9780

pH = 3, $NaClO_4$ 0.1 M, λ > 360 nm,		k	0.17	0.017	
	Anodic WO_3	a	1.01	0.065	0.9120
		k	0.14	0.030	
	Suspension	a	0.99	0.038	0.9731
		k	0.24	0.023	
ATN, with an applied bias of 1.5 V pH = 3, $NaClO_4$ 0.1 M, λ > 360 nm,	Colloidal WO3	a	1.01	0.041	0.9899
		k	0.55	0.054	
	Anodic WO_3	a	1.00	0.044	0.9893
		k	0.65	0.071	
ATN, Anodic WO_3 with an applied bias of 1.5 V pH = 6	$NaClO_4$ 0.1 M, λ > 360 nm	a	1.00	0.025	0.9951
		k	0.41	0.025	
	Na_2SO_4 0.1 M, λ > 360 nm	a	0.99	0.019	0.9974
		k	0.44	0.019	
	Na_2SO_4 0.1 M, λ > 420 nm	a	1.08	0.042	0.9633
		k	0.30	0.041	
	Na_2SO_4 0.7 mM, λ > 360 nm	a	1.06	0.043	0.9717
		k	0.42	0.044	
CBZ pH = 3, $NaClO_4$ 0.1 M, λ > 360 nm,	Colloidal WO_3	a	1.02	0.051	0.9369
		k	0.14	0.023	
	Anodic WO_3	a	1.02	0.038	0.9285
		k	0.093	0.016	
	Suspension	a	0.99	0.039	0.9653
		k	0.22	0.023	
CBZ Anodic WO_3 with an applied bias of 1.5 V pH = 6	$NaClO_4$ 0.1 M, λ > 360 nm	a	0.97	0.067	0.9566
		k	0.36	0.058	
	Na_2SO_4 0.1 M, λ > 360 nm	a	0.97	0.046	0.9914
		k	0.33	0.016	
	Na_2SO_4 0.1 M, λ > 420 nm	a	1.04	0.046	0.9414
		k	0.13	0.017	
	Na_2SO_4 0.7 mM, λ > 360 nm	a	1.04	0.065	0.9677
		k	0.34	0.051	

To gain information about the involvement of radical species on the degradation mechanism of these organic targets an EPR-spin trapping study was performed.

3.3 EPR spin trapping investigation

We have very recently demonstrated, by EPR spin trapping experiments [21], that illuminated WO_3 aqueous suspensions generate OH

•

radicals. Interestingly, few seconds irradiation of WO_3 aqueous suspensions containing ATN in the presence of DMPO causes the prompt formation of the quartet (1: 2: 2: 1, $a_N = a_H = 14.8$ G) typical of the trapping of OH

•

radicals (Fig. 3). The same resonance features are found under λ > 420 nm irradiation, clearly confirming the generation of hydroxyl radicals under visible illumination of the semiconductor (Fig. S6 in SI). This result indicates that despite the presence of ATN, photogenerated holes of WO_3 still produce an excess of OH

•

radicals by water oxidation (Scheme 2, Eq. (1)) that are trapped by DMPO (Eq. (2)). However, prolonging the irradiation period, a second signal becomes evident (Fig. 3). It consists of a triplet of doublets (a_N = 15.36 G, a_H = 20.28 G) whose coupling constants values are in agreement with the formation and trapping by DMPO of a carbon centered radical likely coming from ATN or from a hydroxylated intermediate of ATN (Scheme 2, Eqs. (3) and (4)) [32]. Since this kind of adduct is not observed in the absence of ATN, it is plausible that OH

•

radicals have additional reaction pathways in its presence that can lead to the formation and trapping of different radical species. Provided that incident light can be absorbed by the photoactive material, OH

•

are produced independently by the excitation wavelength of the semiconductor, as should be reasonably expected by considering the much slower hole transfer (0.01-1s) [21,33] with respect to fast (subnanosecond) thermalization of the charge carriers to the lowest energy levels corresponding to the band edges of the semiconductor (Scheme 3). Therefore, the degradation pathway is mediated by OH

•

irrespective of the excitation wavelength. As a consequence, the degradation intermediates will be the same both under UV–vis or pure visible frequencies.

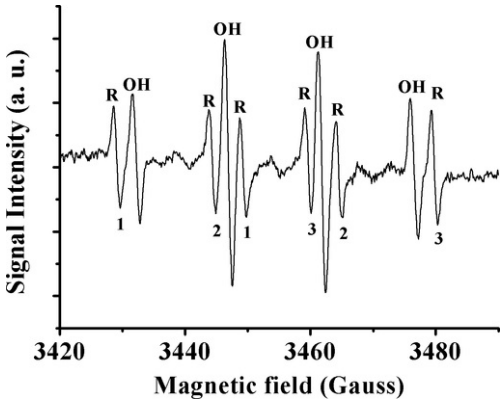

Fig. 3 EPR spin trapping spectrum obtained during irradiation (λ > 360 nm) of a WO_3 aqueous suspension containing ATN (10 mg/L) and DMPO (5×10^{-2} M).

alt-text: Fig. 3

$h^+ + H_2O \longrightarrow OH^{\cdot} + H^+$ (1)

$OH^{\cdot} + DMPO \longrightarrow [DMPO-OH]^{\cdot}$ (2)

$OH^{\cdot} + R \longrightarrow R^{\cdot} + H_2O$ (3)

$R^{\cdot} + DMPO \longrightarrow [DMPO-R]^{\cdot}$ (4)

Scheme 2 Generation of the radical species detected by EPR triggered by hole (h^+) transfer from the semiconductor.

alt-text: Scheme 2

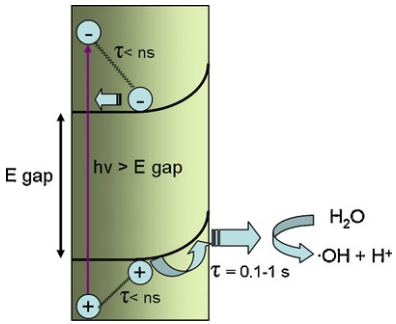

Scheme 3 Generation and thermalization of charge carriers followed by interfacial electron transfer in the 0.1/1 s time domain.

alt-text: Scheme 3

Hydroxyl radicals could follow other reaction pathways in the presence of ATN: i) addition to the organic molecule initiating the oxidative degradation process forming hydroxylated compounds, ii) hydrogen atom abstraction from the drug molecule or from one of the degradation intermediates with formation of a radical then trapped by DMPO (Scheme 2, Eqs. (3) and (4)). The fate of OH

•

radicals is made evident by considering the EPR spin trapping results obtained in the presence of variable concentrations of CBZ (Fig. 4). It is seen that a concentration of CBZ of 10 mg L^{-1} (Fig. 4, red line) causes a decrease of the signal intensity of the adduct [DMPO-OH]

•

and this trend becomes more pronounced by increasing CBZ concentration to 2000 mg L^{-1} (blue line) suggesting that CBZ becomes increasingly competitive with DMPO in capturing photogenerated hydroxyl radicals.

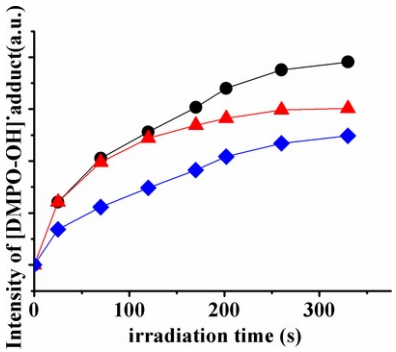

Fig. 4 [DMPO

—

•OH]

•

intensity measured at a fixed field position vs time upon irradiation of WO_3 aqueous suspensions (pH 5.1) containing DMPO (5×10^{-2} M) and $NaClO_4$ (0.1 M) in the absence (●) and in the presence of CBZ 10 mg/L (▲) and 2000 mg/L (♦) respectively. (For interpretation of the references to color in the text, the reader is referred to the web version of this article.)

alt-text: Fig. 4

3.4 Photo-electrocatalytic degradation of drugs by WO_3 electrodes

As the generation of OH

•

radicals by WO_3 is the result of the monoelectronic water photoxidation by holes having a quasi-Fermi potential superior to 2.1 eV vs NHE, the application of a positive potential to WO_3, which is able to support a depletion layer of the length of few tens of nanometers [21,31,34], should increase exponentially the surface concentration of the photoholes, resulting in a parallel increase of the charge transfer rate reflecting the OH

•

production rate at the photoactive interface. Consistent with such interpretation, previous laser flash photolysis experiments indicated that the electron-hole recombination lifetimes were left substantially unchanged, whereas the transient signal assigned to photoholes trapped at the semiconductor surface underwent an exponential increase with applied potential [21]. The selected anodic bias of 1.5 V was indeed that corresponding to the plateau photocurrent originated by the maximum hole transfer rate from the semiconductor to the electrolyte (Figs. S2 and S3 in SI). During this type of photoassisted electrolysis, photogenerated electrons were collected at the ohmic back contact of the photoelectrode and transferred to the counter electrode where hydrogen was evolved. Fig. 5 reports the comparison between the previously presented photocatalytic degradation results (open circuit with disconnected wires (red triangles)) and the photo-electrochemical processes in the cases of ATN, where it can be immediately appreciated the substantial acceleration of the CEC degradation rate under applied potential. The degradation of ATN is almost complete after 5 hrs irradiation under photo-electrocatalytic conditions and also CBZ degradation reaches comparable values (70–80%).

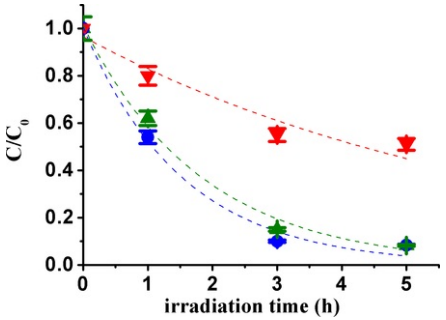

Fig. 5 Degradation of ATN (C_0 = 10 mg/L) dissolved in aqueous solution (pH 3.1) containing $NaClO_4$ (0.1 M) by irradiation (λ > 360 nm) of colloidal WO_3 deposited on FTO (▲) and of anodically grown WO_3 on W foils (●) with an applied bias of 1.5 V vs Pt to the photoanode. Degradation of CBZ (C_0 = 10 mg/L) dissolved in aqueous solution (pH 5.1) containing $NaClO_4$ (0.1 M) by irradiation (λ > 360 nm) of anodically grown WO_3 on W foils with the application of a bias of 1.5 V to the photoanode (▼). Analogous results have been obtained with colloidal WO_3 deposited on FTO. (For interpretation of the references to color in the text, the reader is referred to the web version of this article.)

alt-text: Fig. 5

These results confirm that higher efficiency of the photo-oxidation process (expressed by a ca. fourfold increase in pollutant degradation rate constants, Table 1) can be obtained by exploiting the potential induced increase of surface photohole density. Moreover photogenerated electrons are transferred to the cathodic compartment where, on platinum, trigger protons reduction in acidic environment (protons are also the result of the primary hole scavenging processes according to $H_2O + h^+ \rightarrow OH^{\bullet} + H^+$). As a consequence, their possibility to participate to back recombination reactions involving oxidized CEC intermediates generated at the surface of WO_3 is greatly reduced.

3.5 Identification of organic decomposition intermediates

In order to determine the intermediates formed in the degradation process, samples composed of aliquots withdrawn from photo-electrocatalytic process, at different irradiation time intervals, were analyzed by HPLC–MS/MS.

3.5.1 Atenolol

The fragment ions of ATN intermediates, retention times as well as proposed structures are summarized in Table 2.

Table 2 ATN degradation intermediates, retention times, fragment ions and proposed structures.

alt-text: Table 2

Precursor Ion (m/z)	Retention time (min)	MS^2 (m/z)	Structure
267.17	6.87	225.07	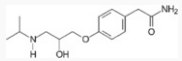
		190.01	
		208.06	

281.15	8.39	116.19 121.08	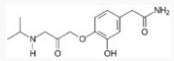
299.16	14.19 15.27	253.04	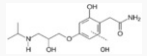
254	12.5	236.20 245.15	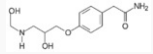
134	2.26	116.10	
132	1.98 2.23	86.06	

The structural assignments of these intermediates were performed on the basis of fragment ions of the MS-MS spectra experimentally determined and compared to those reported in previous studies on ATN degradation [35]. The intermediate having 299 ~~m/z~~ *m/z* was identified as dihydroxylated ATN. The intermediate with 281 ~~m/z~~ *m/z* corresponds to an ATN mono hydroxylated derivative in which the starting alcoholic group of ATN is oxidized to ketone. In order to determine the position of the hydroxyl group, the fragmentation spectra of the oxygenated analog of ATN (~~m/z~~ *m/z* 281) and of ATN were compared. On the basis of the fragmentation pattern we can infer that hydroxylation mainly occurs on the benzene ring of ATN. Other intermediates corresponding to 134, 132 and 152 ~~m/z~~ *m/z* derive from ether chain cleavage and they were identified as 3-(isopropyl amino) propane-1,2-diol, its keto derivative and p-hydroxyphenylacetamide, respectively, on the basis of their fragment ions. Accordingly to literature data ~~[36]~~ [36], the intermediate with 254 ~~m/z~~ *m/z* possibly derives from de-methylation of ATN.

HPLC–MS results show that photodegradation processes are mediated by OH

•

. Indeed, the presence of di-hydroxylated and mono-hydroxylated derivatives are also in agreement with the EPR spin trapping results (vide infra), indicating the possible addition of the hydroxyl radical to ATN (Table 2). Based on the proposed molecular structure of these photoproducts, the photocatalytic degradation of ATN is consistent with the initiation by OH

•

and seems to proceed in a way similar to that already proposed for the TiO_2 catalyzed photodegradation [37]. The identified intermediates were indeed the same as those reported for photo(change "photooxidation" with "photo-oxidation")oxidation processes carried out with other photocatalysts and they have been already proven to be less toxic than the parent molecule, as assessed by toxicity tests [36,37].

Since chemical standards were not available, the overall photo-oxidation process was monitored as peak intensity as a function of the irradiation time. Under our experimental conditions 90% of ATN disappeared after 5 h (pH = 3); prolonging irradiation the peak intensities of all identified intermediates were observed to decrease as shown in Fig. 6 until no residual peaks were detected anymore after 15 h of irradiation, indicating the occurrence of complete mineralization of the organics for sufficiently prolonged irradiation cycles. The evolution of Total Organic Carbon (TOC) with time confirms that the amount of ATN and its intermediates is negligible after 15 h of irradiation (Fig. S7 in SI).

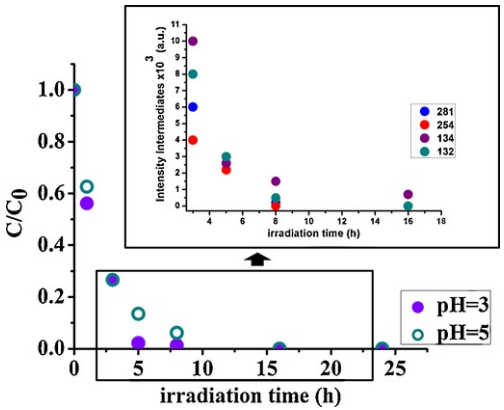

Fig. 6 Degradation of ATN (C_0 = 10 mg/L) in aqueous solutions containing $NaClO_4$ (0.1 M) at either pH 3 or 5 during irradiation (λ > 360 nm) of a WO_3 photoelectrode biased at 1.5 V vs Pt. The chromatographic peak intensity of the degradation intermediates as a function of the irradiation time is reported in the inset (pH 5). See Table 2 for the structures of intermediates classified according to their ~~m/e~~ m/z ratio.

alt-text: Fig. 6

3.5.2 Carbamazepine

The fragment ions of CBZ intermediates, retention times as well as proposed structures are summarized in Table 3.

Table 3 CBZ degradation intermediates, retention times, fragment ions and proposed structures.

alt-text: Table 3

Precursor Ion (~~m/e~~ m/z)	Retention time (min)	MS^2 (~~m/e~~ m/z)	Structure
237.1	14.35	194.01 ~~220.06~~220.06	
251.1	14.5	180.1 ~~208.1223.1~~208.1 223.1	
253.1	12.3	208.0 ~~210.0236.0~~210.0 236.0	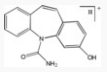
267.1	16.2	168 ~~196.1211.1~~196.1 211.1	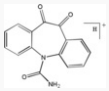
271.1	9.6	210	

	~~253~~253	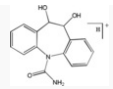

An intermediate corresponding to the molecular weight of a hydroxylated analog of CBZ (253 ~~m/z~~m/z) was detected. Similarly, the 271 ~~m/z~~m/z species was identified as di-hydroxylated CBZ. The fragmentation pattern observed for 251 ~~m/z~~m/z, can be tentatively attributed to a keto derivative of the hydroxylated compound in agreement with Hu et al. [38]. The intermediate 267 ~~m/z~~m/z was identified as diketo-CBZ resulting from the oxidation of hydroxy-groups present in the di-hydroxylated compound (271 ~~m/z~~m/z). Possibly, the transformation of CBZ proceed by different pathways. The major route seems to involve an initial mono-hydroxylation of CBZ followed by oxidation of the hydroxyl group to give mono-keto intermediate (251 ~~m/z~~m/z) or a further hydroxylation step to produce dihydroxy-CBZ (271 ~~m/z~~m/z). The oxidation of one hydroxyl group likely leads to a formation of a hydroxy-keto-intermediate. These HPLC–MS results point out that photodegradation process is mediated by OH

•

also in the case of CBZ. In particular, the presence of mono- and di-hydroxylated CBZ intermediates confirms that the decrease of [DMPO-OH]

•

adduct intensity, observed in EPR spin trapping experiments (vide infra) carried out in the presence of increasing amount of CBZ, is due to a competition between DMPO and CBZ for the reaction with OH

•

.

The hydroxylated intermediates are oxidized through ring-rupturing reactions to aliphatic compounds, which upon further oxidation are mineralized. The peak intensities of the intermediates decrease as the time increases and, likewise the case of atenolol, after 20 h of illumination the mineralization of the drug is obtained (Fig. 7).

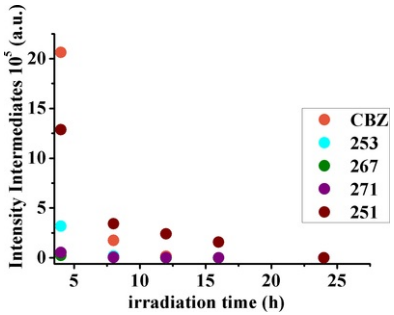

Fig. 7 Exhaustive photo-electrochemical degradation of CBZ at a WO_3 photoanode biased at 1.5 V vs Pt under λ > 360 nm illumination. (C_0 = 10 mg/L, 0.1 M $NaClO_4$ at pH 3.1). See Table 3 for the structures of intermediates classified according to their ~~m/z~~m/z ratio.

alt-text: Fig. 7

It has been reported that some degradation by-products of CBZ can be toxic. In particular, acridine (180 ~~m/z~~m/z) was detected as one of the oxidation products of carbamazepine degradation catalyzed by UV/H_2O_2 [39] or by $BiPO_4$ [40]. However, in the case of our WO_3 driven photo-electrocatalytic process, no intermediate having ~~m/z~~m/z = 180 was observed.

3.6 Photo-electrocatalytic degradation in real conditions

The previous results prompted us to evaluate the photo-electrocatalytic processes in conditions which should be more representative of naturally occurring wastewaters. In particular, in order to ensure WO_3 stability, tests were initially carried out in conditions which are fairly acidic (i.e. pH = 3 for both ATN and CBZ) and in the presence of perchlorate which is known to be a supporting electrolyte with a wide overpotential stability window. The solution composition used for model experiments was therefore quite far from that of either natural waters or domestic wastewaters which, realistically, should undergo the decontamination process. Therefore, it is noteworthy to investigate the applicability of the WO_3 based photo-electro oxidation process on solutions having composition more compatible with naturally occurring environmental conditions.

Fig. 8 shows that the degradation kinetics of ATN and of CBZ obtained in aqueous solution at pH = 6, which should be considered the superior pH limit for the WO_3 stability, in the presence of high (0.1 M) and low (0.7 mM) sodium sulfate concentrations. Although the first order kinetic constant for ATN photodegradation decreases as pH increases (k = 0.65 h^{-1} @ pH = 3 and k = 0.41 h^{-1} @ pH = 6) a degradation of ca 85% of ATN was reached after 5 h irradiation which compares well with the 90% degradation observed at pH 3. On the other hand, the change in the supporting electrolyte composition (from perchlorate to sulfate salts) has a negligible impact on the photodegradation

kinetics of ATN and their difference at long irradiation time (>3 h) is not statistically significant (Table 1). Sulfate was chosen in this experiment since it is found almost universally in natural waters at concentrations ranging from a few tenths to several thousand mg/L, with the highest concentrations usually found in groundwater. The concentration employed in our experiments (0.1 M) was greater than that commonly found in aquatic environments [41], however high levels of sulfate can be efficiently removed in conventional wastewater treatment plants [42].

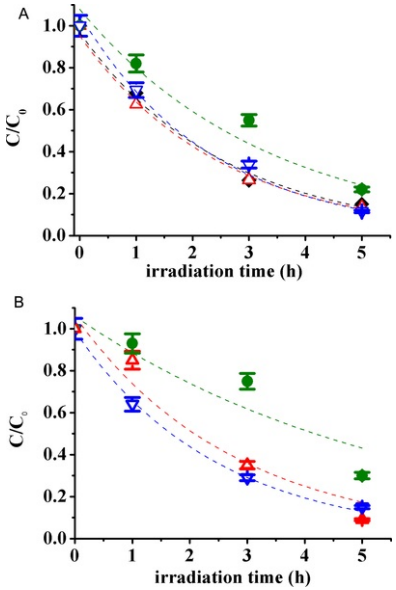

Fig. 8 A) Photo-electrocatalytic degradation (λ > 360 nm) of ATN (C_0 = 10 mg/L) in aqueous solutions (pH 6) containing: $NaClO_4$ (0.1 M) by irradiation (♦), Na_2SO_4 (0.1 M) (△), Na_2SO_4 (0.7 mM) (▽), Na_2SO_4 (0.1 M) (λ > 420 nm) (●). B) Photo-electrocatalytic degradation (λ > 360 nm) of CBZ (C_0 = 10 mg/L) in aqueous solutions (pH 6) containing: Na_2SO_4 (0.1 M) (△), Na_2SO_4 (0.7 mM) (▽), Na_2SO_4 (0.1 M) (λ > 420 nm) (●).

alt-text: Fig. 8

Nonetheless, to investigate the effect of salinity on the photo-electrocatalytic process, a solution containing 200 mg/L of salt (i.e. 0.7 mM), which correspond to total salinity lower than the limit of 500 mg/L recognized as acceptable for freshwater [43], was carried out. Interestingly, despite a ca. 5 fold reduction in the photocurrent flowing across the photo-electrochemical cell (Fig. S8 in SI), the decay rate of both ATN and CBZ is not significantly affected by the decreased ionic strength and cell conductivity at the 0.7 mM Na_2SO_4 concentration at pH 6 (Fig. 8 and Table 1), yielding degradation kinetic parameters similar to those obtained in 0.1 M Na_2SO_4. Evidently, even under diluted electrolyte conditions, the applied bias (1.5 V) is still effective in countering charge recombination by spatially separating photogenerated holes and electrons. As a result, OH$^{\bullet}$ radicals are still produced at a sufficient rate to achieve the primary degradation of the parent contaminants (present in 10 ppm concentration) on a timescale comparable to that observed in a much more concentrated supporting electrolyte solution. In our opinion, this is an important observation, which points to the advantageous applicability of the photo-electrochemical decontamination method even in circumstances where the photocurrent generation is far from being optimized, like those naturally occurring in most freshwaters samples. Clearly, when the electrolyte concentration is further reduced to less than 0.1 mM, the photocurrent under 1.5 V vs Pt further drops to few tens of μA/cm^2 (Fig. S8 in SI) and the photo-electrochemical degradation rate approaches that found under open circuit conditions. This is also reasonable, considering that in this limiting case, due to very poor conductivity (and thus large cell resistance (KΩ)) only a small fraction of electrons is able to leave the semiconductor for flowing through the external circuit and escaping recombination with the positive charge carriers.

Finally, we would like to stress that WO_3 represents a good compromise between band edge energy levels which are suitable to drive demanding oxidation reactions, such as monoelectronic water oxidation, and sun harvesting capabilities, allowing to capture visible photons up to 460–480 nm. From this point of view WO_3 can be much more efficient in oxidative photo-electro catalytic cycles than undoped anatase. In fact, no photocatalytic activity was obtained with undoped TiO_2 for λ > 420 nm, at which the WO_3 electrodes still show a sizable absorption and photoconversion (Figs. S9 and S10 in SI). Although, as expected, the degradation kinetics of the two target molecules obtained with a 420 nm cut-off filter are slower, due to the small visible absorption coefficient of the indirect band gap $WO_{3,}$ (change WO_3 with WO_3,) (Table 1 and Fig. 8). (change "." with ",") T (change "The" with "the")he degradation rate constants ($k = 0.30\ h^{-1}$ and $k = 0.13\ h^{-1}$ at pH = 6, under visible light for ATN and CBZ respectively) are still significant, in agreement with the photoaction spectrum taken at 1.5 V (IPCE ca. 20%, Fig. S10), confirming a significant response of the photoelectrode in the visible region and the real applicability of photo-electro remediation of pollutants on WO_3 under solar irradiation.

4 Conclusions

Much work has been done in past years on the photocatalytic degradation of organic pollutants on titanium dioxide, testifying that the technology can be applied to a wide spectrum of recalcitrant organic pollutants. One of the main limitations of native TiO_2 is the poor response under visible light, due to its large band gap of the order of 3.2 eV.

In this work, we explored the possibility to carry out near UV–vis photodegradation experiments of environmentally relevant target molecules like atenolol (ATN) and carbamazepine (CBZ), representing both indicator compounds and potentially hazardous recalcitrant CECs, by using nanocrystalline WO_3. The present study was mainly focused on the exploitation of micrometer-thick WO_3 films, either obtained by colloid sintering on FTO or by electrochemical anodization of tungsten. These films are able to absorb visible light up to 470 nm and to generate OH

•

radicals via valence band injection of long lived holes, promoting the OH

•

mediated oxidation of most organic species. The identification of a series of hydroxylated decomposition intermediates produced from both ATN and CBZ, are consistent with such degradation mechanism. In general, the ability to photodegrade the organic pollutants under consideration was found to proceed at comparable rate for both WO_3 powder suspensions and supported thin films (photoelectrodes) under open circuit (photocatalytic conditions). However, in the case of WO_3 electrodes, a considerable acceleration of the degradation kinetics (up to 4–5 times) was obtained through the application of a potential bias, instrumental to optimize the charge separation within the thin films and to maximize the hole transfer rate to the electrolyte. Moreover, for sufficiently long illumination times the photo-electrochemical route led to disappearance of all the intermediate decomposition products of the selected CECs, indicating the complete mineralization of each respective pollutant. Even in conditions where the photocurrent generation was not optimized, like diluted supporting electrolyte (0.7 mM), representing the average salinity of natural freshwater samples, the photo-electrochemical degradation process (applied bias condition) preserved its effectiveness and a large efficiency margin over conventional open circuit photocatalysis, demonstrating the advantageous practical feasibility of the photo-electrochemical approach. Work is now directed towards the design and fabrication of photo-electrochemical reactors which will be able to maximize light harvesting, operating under optimized flow conditions and under solar concentration.

Acknowledgements

Funding from the ~~University of Ferrara~~University of Ferrara (multidisciplinary projects-PRIA) is gratefully acknowledged. We are grateful to Mr. Gabriele Bertocchi for the technical assistance XRD analysis.

Appendix A. Supplementary data

Supplementary data associated with this article can be found, in the online version, at http://dx.doi.org/10.1016/j.apcatb.2016.11.007.

References

[1] M.X. Tan, P.E. Laibnins, S.T. Nguyen, J.M. Kesselman, C.E. Stanton and N.S. Lewis, *Prog. Inorg. Chem.* **41**, 1994, 21–144.

[2] M.G. Walter, E.L. Warren, J.R. McKone, S.W. Boettcher, Q. Mi, E.A. Santori and N.S. Lewis, *Chem. Rev.* **110**, 2010, 6446–6473.

[3] C.A. Bignozzi, S. Caramori, V. Cristino, R. Argazzi, L. Meda and A. Tacca, *Chem. Soc. Rev.* **42**, 2013, 2228–2246.

[4] K.R. Reyes-Gil, C. Wiggenhorn, B.S. Brunschwig and N.S. Lewis, *J. Phys. Chem. C* **117**, 2013, 14947–14957.

[5] C. Santato, M. Odziemkowski, M. Ulmann and J. Augustynski, *J. Am. Chem. Soc.* **123**, 2001, 10639–10640.

[6] C. Santato, M. Ulmann and J. Augustynski, *J. Phys. Chem. B* **5**, 2001, 936–940.

[7] R. Solarska, B.D. Alexander and J. Augustynski, *J~~ournal of~~. Solid State Electrochem~~istry~~.* **8**, 2004, 748–756.

[8] J.H. Park and A.J. Bard, *Electrochem~~ical and Solid-State Letter~~s. Solid State Lett.* **9**, 2006, E5–E8.

[9] L. Meda, G. Tozzola, A. Tacca, G.L. Marra, S. Caramori, V. Cristino and C.A. Bignozzi, *Sol~~ar Energy Materials and Solar~~. Energy Mater. Sol. Cells* **94**, 2010, 788–796.

[10] N.R. de Tacconi, C.R. Chenthamarakshan, G. Yogeeswaran, A. Watcharenwong, R.S. de Zoysa, N.A. Basit and K. Rajeshwar, ~~*The Journal of Phyisical Chemistry B110200625347-22355*~~*J. Phys. Chem. B* **110**, 2006, (25347-22355).

[11] A. Watcharenwong, W. Chanmanee, N.R. de Tacconi, C.R. Chenthamarakshan, P. Kajitvichyanukul and K. Rajeshwar, *Journal of Electroanalytical Chemistry, Electroanal. Chem.* **612**, 2008, 112.

[12] R. Hahn, J.M. Macak and P. Schmuki, *Electrochemistry Communications, Commun.* **2007**, 2007, 947–952.

[13] V. Cristino, S. Caramori, R. Argazzi, L. Meda, G.L. Marra and C.A. Bignozzi, *Langmuir* **27**, 2011, 7276–7284.

[14] P. Delichere, P. Falaras, M. Froment and H.-L. Goff, *Thin Solid Films* **161**, 1988, 35–46.

[15] M.F. Daniel, B. Desbat, J.C. Lassegues and R. Garie, *Journal of Solid State Chemistry, Solid State Chem.* **73**, 1988, 127–139.

[16] A. Rougier, F. Portemer, A. Quédé and M. El Marssi, *Applied Surface Science, Surf. Sci.* **153**, 1999, 1–9.

[17] M. Allaf Behbani, M. Ranjbar, P. Kameli and H. Salamati, *Sens. Actuators B: Chem.* **188**, 2013, 127–136.

[18] G. Leftherotis, S. Papaefthimiou and P. Yianoulis, *Solar Energy Materials and Solar, Energy Mater. Sol. Cells* **83**, 2004, 115–124.

[19] J.K. Kim, K. Shin, S.M. Cho, T.-W. Lee and J.H. Park, *Energy & Environmental ScienceEnviron. Sci.* **4**, 2011, 1465–1470.

[20] Q. Mi, A. Zhanaidarova, B.S. Brunschwig, H.B. Gray and N.S. Lewis, *Energy & Environmental ScienceEnviron. Sci.* **5**, 2012, 5694–5700.

[21] V. Cristino, M. Sabrina, A. Molinari, S. Caramori, S. Carli, R. Boaretto, R. Argazzi, L. Meda and C.A. Bignozzi, *J. Mater. Chem. A* **4**, 2016, 2995–3006.

[22] D.V. Esposito, R.V. Forest, Y. Chang, N. Gaillard, B.M. McCandless, S. Hou, K.H. Lee, R.W. Birkmire and J.G. Chen, *Energy & Environmental ScienceEnviron. Sci.* **5**, 2012, 9091–9099.

[23] K.R. Reyes and D.B. Robinson, WO_3/TiO_2 Nanotube Photoanodes for Solar Water Splitting with Simultaneous Wastewater Treatment, 2013, Sandia National Laboratories, SAND2013-4274(SAND2013-4274).

[24] I. Tantis, E. Stathatos, D. Mantzavinos and P. Lianos, *J. Chem. Technol. Biotechnol.* **90**, 2015, 1338–1344.

[25] I. Tantis, L. Bousiakou, Z. Frontistis, D. Mantzavinos, I. Konstantinou, M. Antonopoulou, G.-A. Karikas and P. Lianos, *J. Hazard. Mater.* **294**, 2015, 57–63.

[26] B. Kasprzyk-Hordern, R.M. Dinsdale and A.J. Guwy, *Water Res.* 2009, 363–380.

[27] M. Jekel, W. Dott, A. Bergmann, U. Dünnbier, R. Gnirß, B. Haist-Gulde, G. Hamscher, M. Letzel, T. Licha, S. Lyko, U. Miehe, F. Sacher, M. Scheurer, C.K. Schmidt, T. Reemtsma and A.S. Ruhl, *Chemosphere* **125**, 2015, 155–167.

[28] M.J. Benotti, R.A. Trenholm, B.J. Vanderford, J.C. Holady, B.D. Stanford and S.A. Snyder, *Environmental Science & Technology, Sci. Technol.* **43**, 2008, 597–603.

[29] M.S. Kostich, A.L. Batt and J.M. Lazorchak, *Environmental Pollution, Pollut.* **184**, 2014, 354–359.

[30] F. Angiuli, R. Argazzi, S. Caramori and C.A. Bignozzi, A Method for Preparing Nanocrystalline Transparent Films of Tungsten Oxide, 2007, PCT/IT2006/000084(PCT/IT2006/000084).

[31] A. Tacca, L. Meda, G. Marra, A. Savoini, S. Caramori, V. Cristino, C.A. Bignozzi, V. Gonzalez Pedro, P.P. Boix, S. Gimenez and J. Bisquert, *ChemPhysChem* **13**, 2012, 3025–3034.

[32] G.R. Buettner, *Free Radic. Biol. Med.* **3**, 1987, 259–303.

[33] M. Pesci, A.J. Cowan, B.D. Alexander, J.R. Durrant and D.R. Klug, *J. Phys. Chem. Lett.* **2**, 2011, 1900–1903.

[34] S.R. Biaggio, R.C. Rocha-Filho, J.R. Vilche, F.E. Varela and L.M. Gassa, *Electrochim. Acta* **42**, 1997, 1751–1758.

[35] C. Medana, P. Calza, F. Carbone, E. Pelizzetti, H. Hidaka and C. Baiocchi, *Rapid Commun. Mass Spectrom.* **22**, 2008, 301–313.

[36] L.A. Ioannou, E. Hapeshi, M.I. Vasquez, D. Mantzavinos and D. Fatta-Kassinos, *Sol. Energy* **85**, 2011, 1915–1926.

[37] V. Píšťková, M. Tasbihi, M. Vávrová and U.L. Štangar, *Journal of Photochemistry and Photobiology A: Chemistry, Photochem. Photobiol. A: Chem.* **305**, 2015, 19–28.

[38] L. Hu, H.M. Martin, O. Arce-Bulted, M.N. Sugihara, K.A. Keating and T.J. Strathmann, *Environmental Science & Technology. Sci. Technol.* **43**, 2016, 509–515.

[39] O.S. Keen, S. Baik, K.G. Linden, D.S. Aga and N.G. Love, *Environmental Science & Technology. Sci. Technol.* **46**, 2012, 6222–6227.

[40] J. Xu, L. Li, C. Guo, Y. Zhang and W. Meng, *Applied Catalysis B: Environmenta. Catal. B: Environ.* **130**, 2013, 285–292.

[41] http://water.usgs.gov/edu/saline.html.

[42] S.M. García-Solares, A. Ordaz, O. Monroy-Hermosillo, J. Jan-Roblero and C. Guerrero-Barajas, *Applied Biochemistry and Biotechnology. Biochem. Biotechnol.* **174**, 2014, 2919–2940.

[43] https://www3. epa.gov/caddis/ssr_ion_int.html-.

Appendix A. Supplementary data

The following is Supplementary data to this article:

Multimedia Component 1

Graphical abstract

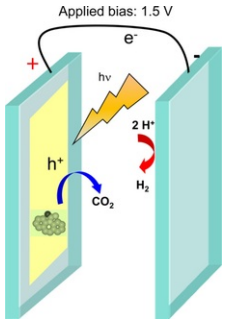

Highlights

- Photoexcited WO_3 is active in the degradation of pharmaceuticals in water.
- Bias application on photoexcited WO_3 electrodes accelerate degradation kinetics.
- Photo-electrodegradation process passes through OH
  radicals formation.
- Prolonged irradiation allows complete mineralization of pharmaceuticals.
- Photo-electrocatalytic method works at pH 6 and with salinity of natural waters.

Queries and Answers

Query: The author names have been tagged as given names and surnames (surnames are highlighted in teal color). Please confirm if they have been identified correctly.
Answer: Surnames are correctly typed

Query: Please check the country name in affiliation and correct if necessary.
Answer: Affiliation and country name are ok

Query: “Your article is registered as a regular item and is being processed for inclusion in a regular issue of the journal. If this is NOT correct and your article belongs to a Special Issue/Collection please contact e.mohan@elsevier.com immediately prior to returning your corrections.”
Answer: It is correct

Query: One or more sponsor names and the sponsor country identifier may have been edited to a standard format that enables better searching and identification of your article. Please check and correct if necessary.
Answer: Yes the typing is correct

Query: Please check author names in Ref. [39] and correct if necessary.
Answer: ref 39 is correct

Query: Figs. 4 and 5 will appear in black and white in print and in color on the web. Based on this, the respective figure captions have been updated. Please check, and correct if necessary.
Answer: OK

Query: Please check the presentation of tables and correct if necessary.
Answer: tables are ok